Interference of two-photon transitions induced by XUV light

Matjaž Žitnik, Andrej Mihelič, Klemen Bučar, Špela Krušič, Richard Squibb, Raimund Feifel, Iyas Ismail, Pascal Lablanquie, Jérôme Palaudoux, Oksana Plekan, et al.

OPTICA

Interference of two-photon transitions induced by XUV light

M. Žitnik,[1,2,*] A. Mihelič,[1,2] K. Bučar,[1,2] Š. Krušič,[1,2] R. Squibb,[3] R. Feifel,[3] I. Ismail,[4] P. Lablanquie,[4] J. Palaudoux,[4] O. Plekan,[5] M. Di Fraia,[5] M. Coreno,[5,6] M. Manfredda,[5] A. Simoncig,[5] P. Rebernik Ribič,[5,7] F. Sottocorona,[5] E. Allaria,[5,8] K. C. Prince,[5] C. Callegari,[5] and F. Penent[4]

[1]Jožef Stefan Institute, Jamova cesta 39, SI-1000, Ljubljana, Slovenia
[2]Faculty of Mathematics and Physics, University of Ljubljana, Jadranska 19, SI-1000 Ljubljana, Slovenia
[3]Department of Physics, University of Gothenburg, SE-412 96, Gothenburg, Sweden
[4]LCP-MR (UMR 7614), Sorbonne Université and CNRS, 4 Place Jussieu, F-75005, Paris, France
[5]Elettra-Sincrotrone Trieste, Strada Statale 14-km 163.5, I-34149, Basovizza Trieste, Italy
[6]Consiglio Nazionale delle Ricerche–Istituto di Struttura della Materia, LD2 unit, 34149, Trieste, Italy
[7]Laboratory of Quantum Optics, University of Nova Gorica, Nova Gorica, 5001, Slovenia
[8]Current address: Deutsches Elektronen-Synchrotron DESY, Notkestrasse 85, 22607, Hamburg, Germany
*Corresponding author: matjaz.zitnik@ijs.si

Received 1 November 2021; revised 17 May 2022; accepted 18 May 2022; published 24 June 2022

The relative phase of first (ω_1) and third harmonics (ω_3) extreme ultraviolet light pulses was varied to control the population of the $2s^2$ state in helium through the interference of $\omega_1+\omega_1$ and $\omega_3-\omega_1$ two-photon excitation paths. The population was monitored by observing the total electron yield due to the $2s^2$ autoionization decay. Maximum yield occurs when the relative phase of the two harmonics matches the phase difference of complex atomic amplitudes governing the two excitation paths. The calculated trend of atomic phase differences agrees well with the measured data in the spectral region of the resonance, provided that time-reversed $-\omega_1+\omega_3$ path is also taken into account. These results open the way to accessing phase differences of two-photon ionization paths involving energetically distant intermediate states and to perform interferometry in the extreme ultraviolet range by monitoring final state populations.

https://doi.org/10.1364/OPTICA.447436

1. INTRODUCTION

With the advent of coherent light sources generating high-order odd-harmonics (HHG) ω_{2n-1} of a driving infrared (IR) laser frequency ω_1 [1], two-photon above-threshold ionization (ATI) has attracted much attention due to the attosecond temporal sensitivity displayed by the so-called reconstruction of attosecond beating by interference of two-photon transitions (RABBITT) technique [2–4]. This is based on beating of the photoelectron yield from an atomic shell with ionization potential T_p at electron kinetic energy $\omega_{2n}-T_p$ due to interference of indistinguishable $\omega_{2n-1}+\omega_1$ and $\omega_{2n+1}-\omega_1$ two-photon ionization paths and is observed by varying the delay of the phase-locked IR pulse with respect to the pulse of the extreme ultraviolet (XUV) light emitted by the HHG source. The measurement is done at many neighboring pairs of odd harmonic frequencies simultaneously, and identification of delays at which different electronic sidebands ω_{2n} show their maximum yield has allowed determination of Wigner time delay difference for nonresonant photoionization of different atomic subshells [5–7]. The established extraction procedure involves subtraction of the so-called continuum–continuum phase from the measured two-path phase difference [8]. This extra phase is induced by the interaction of IR light with a photoelectron in the region dominated by the $Z=1$ Coulomb potential of the ion, and can be handled for any atomic target by using analytical approximations derived from the asymptotic form of the two-photon matrix element.

In fact, the RABBITT scheme represents an extension of all-optical coherent control experiments pioneered by Brumer, Shapiro, and others [9–11], where one of the photons in the multicolor excitation path is replaced by an XUV photon. The technique is readily implemented by combining weak coherent XUV light pulses with the laser probe of moderate intensity because of the relatively strong interaction of IR light with the electronic continuum. An interesting and not yet fully analyzed situation arises when the IR probe photons are substituted by XUV photons, leading, for example, to the simplest $\omega_1+\omega_1$ and $\omega_3-\omega_1$ RABBITT type two-photon interference scheme involving XUV photons only. As indicated by the ω^{-2} dependence of the electron kinetic energy, the interaction of XUV photons with an electronic continuum is at least 2 orders of magnitude weaker than the IR photon

interaction. Thus, to investigate the potential of such an XUV-RABBITT scheme, multicolor and tunable sources of intense and coherent XUV light are required.

The last decade has seen a rapid development of free-electron laser (FEL) sources [12], and especially seeded FELs operating at XUV wavelengths hold the potential to fulfill the above requirements [13]. This is indicated by several recent studies observing the effects of the competing two-photon ($\omega_1+\omega_1$) and one-photon (ω_2) ionization paths on the photoelectron angular distribution [14,15]. Although the opposite parity transfer along the two concurrent ionization paths prevents control of the final state populations, these experiments already are an all-XUV upgrade of similar optical studies from the 1990s [16–20] and have successfully solved some technical challenges specifically emerging at shorter wavelengths. For example, it is important to delay one XUV light pulse with respect to the other with a temporal resolution equal to a fraction of one optical period of the higher frequency in the two-color excitation scheme. At seeded FELs, the two XUV harmonic components are produced by two distinct undulator modules, and delay is provided by a small chicane that slightly lengthens the path of the light-generating electron bunch between the modules [21]. Using such a technique, 0.9 as resolution of delay between the ω_1 and ω_2 light pulses was achieved, leading to 0.2 rad phase sensitivity at 31.5 nm [14].

When dealing with two-color two-photon excitations, high intensity of both XUV colors is required to balance the probabilities of $\omega_1+\omega_1$ and $\omega_3-\omega_1$ ionization paths. Optimally, the intensity I_3 of the third harmonic needs to be higher than intensity I_1 of the fundamental in order to compensate for the lower photoionization cross section at higher photon energy and for the weaker interaction of the ω_1 radiation field with the faster photoelectron. However, the number of FEL undulators for generation of light of each color is necessarily smaller than in the single-color case, and at present, such experiments are feasible only when the final state is a resonance embedded in the electronic continuum. Consequently, the photon energy $\omega_1=\omega_3/3$ is limited to the vicinity of $E_r/2$, where E_r is the excitation energy of the selected resonant state, and the phase difference of the two-photon ionization paths is strongly affected by the nature of the quasi-bound final state. This is similar to numerous (RAINBOW) RABBITT studies with one of the XUV harmonics tuned to a specific group of intermediate bound [22] or resonance states [23–27]. This situation prompted the development of dedicated numerical models to interpret the data [28–31], and the same applies for the present XUV-RABBITT experiment with an extra challenge: the presence of two XUV photons of different colors in one of the ionization paths reopens the question of whether the contribution of the time-reversed $-\omega_1+\omega_3$ path remains negligible, as safely assumed for conventional RABBITT experiments, with ω_1 in the IR spectral region [8].

We have employed the $\omega_1+\omega_1$ and $\omega_3-\omega_1$ interference scheme to control the population of the $2s^2\,{}^1S^e$ autoionizing state in helium (He), which has a characteristic lifetime of 5 fs (Fig. 1). The theoretical parametrization of such an XUV-RABBITT process is given below together with the link establishing the correspondence with the typical RABBITT analysis. The present report continues with a brief description of the experimental setup and methods to collect the data for comparison with the theory, first looking at the single-color two-photon ionization profile of the resonance, and finally presenting the two-color phase-sensitive results.

2. THEORY

A. Parameterization of the Two-Photon Ionization Rate

To describe resonant two-photon ionization, we use the formalism introduced by Fano [32], generalized to absorption of two photons [33,34]. When an He atom is irradiated by the fundamental alone (diagram A in Fig. 1), the two-photon ionization rate may be written as

$$R_< = \frac{\pi}{2}\left|F_1^2\mu_s^<\frac{x+q_<}{x+i}\right|^2+\frac{\pi}{2}|F_1^2\mu_d^<|^2, \tag{1}$$

where $x=2(2\omega_1-E_r)/\Gamma_r$, $E_r\approx 2.12586$ a.u. (57.848 eV) is the excitation energy of $2s^2\,{}^1S^e$ resonance, $\Gamma_r\approx 4.54\times10^{-3}$ a.u. (123 meV) the autoionization width [35], $\mu_s^<$ and $\mu_d^<$ are the two-photon $\omega_1+\omega_1$ transition amplitudes to the $1s\epsilon s$ and $1s\epsilon d$ continua, F_1 is the slowly varying electric field envelope, and $q_<$ is the (generalized) Fano parameter. The first term in Eq. (1) describes the transition to the $1s\epsilon s$ continuum, in which the $2s^2$ resonance state is embedded, and the second term describes the transition to the nonresonant $1s\epsilon d$ continuum. Note that, in contrast with one-photon ionization, the Fano parameter is complex in the present case [33,34].

When both the fundamental and the third harmonic are present, the amplitudes in Eq. (1) are replaced with the sums of the amplitudes corresponding to diagrams A, B, and B′ in Fig. 1. Diagrams B and B′ depict, respectively, absorption of the third harmonic, followed by stimulated emission of the fundamental ($\omega_3-\omega_1$), and stimulated emission of the fundamental, followed by absorption of the third harmonic ($-\omega_1+\omega_3$). The resulting overall two-photon ionization rate is

$$R_{<>} = \frac{\pi}{2}\left|F_1^2\mu_s^<\frac{x+q_<}{x+i}+e^{i\phi}F_1F_3\mu_s^>\frac{x+q_>}{x+i}\right|^2$$
$$+\frac{\pi}{2}|F_1^2\mu_d^<+e^{i\phi}F_1F_3\mu_d^>|^2, \tag{2}$$

where $q_>$, $\mu_s^>$, and $\mu_d^>$ are the Fano parameter, and the $1s\epsilon s$, and $1s\epsilon d$ transition amplitude associated with the sum of both

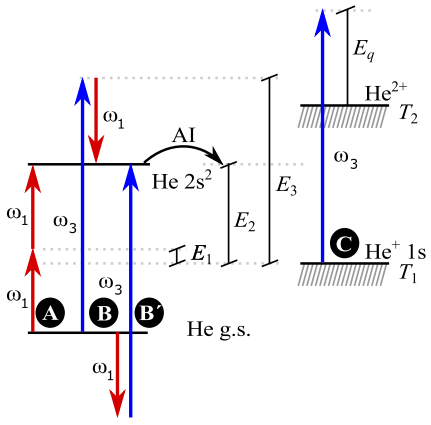

Fig. 1. Left, two-photon excitation to the $2s^2$ autoionizing state in He with the fundamental (ω_1, short vertical arrow) and the third harmonic (ω_3, long vertical arrow). Path A, two-photon $\omega_1+\omega_1$ excitation; path B, two-photon $\omega_3-\omega_1$ excitation; path B′ (time-reversed path B): two-photon $-\omega_1+\omega_3$ excitation; AI, autoionization decay. Right, single-photon ionization of the ground-state He^+ ion by the third harmonic (path C). The kinetic energies of the ejected electrons are denoted by E_1, E_2, E_3, and E_q. The ionization thresholds of the He ground state (g.s.) atom and He^+ 1s ion are labeled by T_1 and T_2, respectively.

diagrams B and B′. In Eq. (2), ϕ denotes the tunable phase shift between the carrier waves of the fundamental and the third harmonic, and F_1 and F_3 are the corresponding field envelopes.

The two-photon ionization of an He atom in the ground state is described by the following set of parameter values (in atomic units) in the energy region of the $2s^2\,{}^1S^e$ resonance,

$$q_< = -7.24 - i5.43, \tag{3a}$$

$$q_> = -2.10 + i1.43, \tag{3b}$$

$$|\mu_s^<| = 0.47 \text{ a.u.}, \tag{3c}$$

$$|\mu_d^<| = 0.65 \text{ a.u.}, \tag{3d}$$

$$\mu_s^>/\mu_s^< = 0.41 + i0.16, \tag{3e}$$

$$\mu_d^>/\mu_d^< = 0.143 + i0.015. \tag{3f}$$

The two-photon background ionization cross sections associated with $\mu_s^<$ and $\mu_d^<$ are approximately 0.0033 a.u.(0.63×10^{-52} cm^4 s) and 0.0067 a.u. (1.28×10^{-52} cm^4 s). The above parameters have been extracted from the partial photoionization amplitudes, which have been obtained in a high-precision first-principles calculation [36,37].

It should be stressed that in the two-color case, a gauge-independent result was obtained only when amplitudes for both diagrams (B and B′) were included in the calculation. In this case, very good agreement between the length and velocity form [38] was obtained for both the s and d partial waves. This is different from the RABBITT scheme, where the contribution of the IR emission–XUV absorption process is negligible compared to the contribution from the time-reversed process [8], at least at laser intensities where electrons mostly exchange a single photon with the IR field [39]. Specifically, we have found that, in the He $2s^2\,{}^1S^e$ resonance region, the inclusion of the B′ amplitude causes a change of up to 30–40% of the magnitude and phase of the two-color two-photon matrix element.

Under the present experimental conditions, the incident pulses are 50 fs (FWHM) long, so that the fields complete many optical cycles, and their envelopes vary slowly on the time scale of the optical periods. Since the spectral width is small compared to Γ_r, the electron yield may be calculated by multiplying rates $R_<$ and $R_{<>}$ with the effective pulse duration (t_{eff}) because, in the present treatment, field envelopes of the first- and the third-harmonic pulses fully overlap in time. It should be noted that a description in terms of a transition rate is applicable only when the transition is not saturated. Indeed, two-photon Rabi flopping is suppressed in our case because of strong one-photon ionization of the ground-state atoms.

For each photon energy ω_1, Eq. (2) enables the calculation of the phase angle at which the two-path interference results in the maximum electron yield from the autoionization. In fact, the single-atom electron yield $t_{\text{eff}} R_{<>}$ can be written as

$$y(\omega_1, \phi) = |F_1^2 M_< + F_1 F_3 e^{i\phi} M_> e^{-i\delta}|^2, \tag{4}$$

where $M_<$ and $M_>$ are positive quantities, and δ is a phase angle. While a general expression for δ can be deduced from Eq. (2), note that, in the $2s^2\,{}^1S$ resonance region, the electron yield is dominated by the first term of Eq. (2). As a consequence, $\delta \approx \delta_s$, where δ_s denotes the phase difference between the one- (A) and two-color

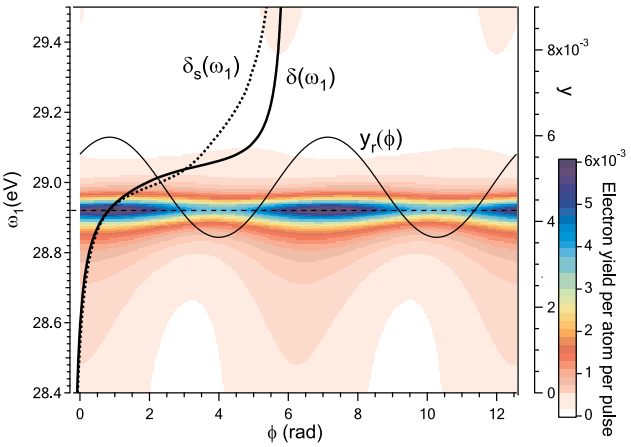

Fig. 2. Electron yield y as a function of the fundamental frequency ω_1 and phase difference ϕ between the third and the first harmonic calculated from Eq. (2) for pulse duration $t_{\text{eff}} = 50$ fs and harmonic intensities $I_1 = I_3 = 10^{13}$ W/cm^2. The cosine-modulated yield $y_r(\phi)$ (thin solid curve, right axis) with ω_1 set to the top of the $2s^2$ resonance (thin dashed line) is also plotted. At a given fundamental, the electron yield reaches maximum value at $\phi = \delta(\omega_1)$. The calculated δ (from Eq. (9), thick black curve) practically coincides with the atomic phase difference δ_s in the final electronic s wave channel (the first term in Eq. (2), thick dashed curve) except at large frequency detuning where the nonresonant d wave contribution becomes important.

(B and B′) complex atomic amplitudes of the s-wave channel (Fig. 2). According to Eq. (9), the maximum yield is expected for $\phi = \delta$. The calculated phase difference δ displays a 2π jump when ω_1 changes across the resonance (Fig. 2). It is clear that the interference effects persist off-resonance in the $1s\epsilon s$ and $1s\epsilon d$ continuum, but the electron yield there is expected to reach only about 1% of the maximum on-resonance yield. Another consequence of the interference is that the effective Fano parameter (i.e., the line profile) depends on the tunable phase ϕ.

While the phase angle δ does not depend on the light intensity ratio $I_3/I_1 = F_3^2/F_1^2$, the visibility of interference does. This is quantified in terms of the interference contrast,

$$\eta = (y_{\max} - y_{\min})/y_{\max}, \quad 0 \le \eta \le 1, \tag{5}$$

which is derived from the maximum ($y_{\max}$) and the minimum ($y_{\min}$) electron yield observed in a scan over ϕ. A higher contrast means that the cosine modulation is more pronounced due to the two-photon interference. When the excitation energy is tuned to the top of the resonance, the maximum contrast ($\eta = 1$) is expected when $I_3/I_1 \approx 60$ because at equal intensities of the two harmonics, ionization via pathway A is more probable than ionization via pathways B + B′ by the same factor, i.e., $M_</M_> \approx \sqrt{60}$ in Eq. (4). Away from the maximum, the contrast falls off steadily and is predicted to stay above 10% in a range of I_3/I_1, spanning 5 orders of magnitude. An increase of the frequency detuning, $2\omega_1 - E_r$, shifts the maximum contrast toward higher value of the intensity ratio.

B. Comparison of XUV-RABBITT with RABBITT and the Hydrogen Limit

The continuum–continuum phase (ϕ_{cc}) refers to the phase shift experienced by a quasi-free electron due to interaction with the radiation field. It can be obtained from the exact phase of the

two-photon ionization amplitude by subtracting the phase due to the one-photon absorption in the first step of ionization [8]. When ϕ_{cc} can be reliably estimated, the phase difference between single-photon ionization amplitudes can be extracted from the phase difference between the two-photon ionization paths, which is measured using the RABBITT technique. Dahlström and coauthors [8] give a useful analytical approximation for ϕ_{cc} for the hydrogen atom if the electron kinetic energy in the final Coulomb continuum state is larger than the photon energy. We have reproduced their results with a fully numerical calculation (see Fig. 3 in Ref. [8]). There is also no doubt about the applicability of this approximation to other targets too when dealing with 1.55-eV photons from a typical RABBITT setup.

An interesting question is whether the ϕ_{cc} phase for He can still be estimated by the continuum–continuum phase of the equivalent nonresonant two-photon ionization amplitude in hydrogen if the photon energy is in the XUV region. Here, "equivalent" means that the frequencies of the two colors in the ionization pathway of hydrogen are selected so that electron kinetic energies in the intermediate and final continuum states match the corresponding kinetic energies in the selected two-photon ionization pathway in He. Considering an extra phase shift due to the short range atomic potential in He, these two phases should be approximately equal because the second (nonresonant) photoionization step connects approximately the same initial and final continuum states. The difference in the He and H $1s$ ionization potentials ($\Delta T = 10.982$ eV) translates the $\omega_1 + \omega_1$ and $\omega_3 - \omega_1$ ionization pathways in He to the equivalent two-color $(\omega_1 - \Delta T) + \omega_1$ and $(\omega_3 - \Delta T) - \omega_1$ pathways in hydrogen. The results of our calculations in Fig. 3 show that ϕ_{cc} in He is indeed well reproduced by the continuum–continuum phase from the equivalent hydrogen case except, of course, in the resonance region, where the admixture of the localized component (the discrete state) is strong; while the nonresonant background is describable in the single active electron approximation, this does not hold for a resonant continuum. We note that the analytical formulas for ϕ_{cc} given previously {Eqs. (22) and (30) in Ref. [8]} are not applicable in the present case because the photoelectron in the intermediate state has relatively low kinetic energy (<5 eV), and a fully numerical calculation of the two-photon ionization amplitude is required for pathway A, even for the hydrogen atom.

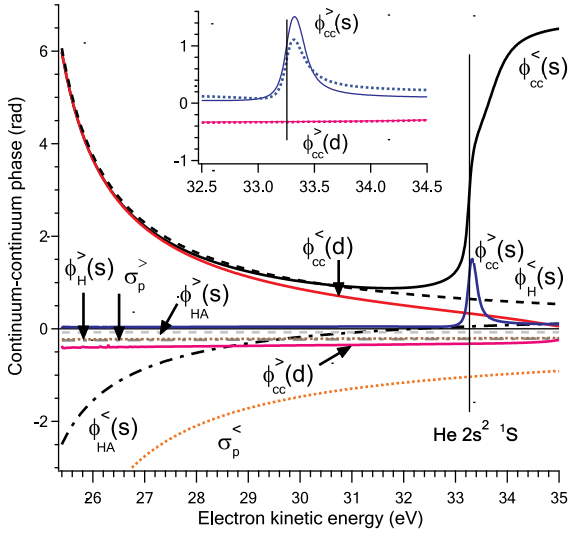

Fig. 3. Calculated continuum–continuum phases $\phi_{cc}^{<}(\ell)$ and $\phi_{cc}^{>}(\ell)$ for pathway A and pathway(s) B + B′ as functions of the kinetic energy of the ejected electron ($\ell = s, d$). The phases include a contribution from autoionization of the $2s^2\,{}^1S^e$ resonance and are compared to $\phi_H^{<}(s)$ and $\phi_H^{>}(s)$, the accurate continuum–continuum phases from the equivalent two-photon ionization of hydrogen, and to analytical approximations $\phi_{HA}^{<}(s)$ and $\phi_{HA}^{>}(s)$ given by Eq. (22) of Ref. [8]. The one-photon phases of p electrons with kinetic energies $\omega_1 - \Delta T$ and $\omega_3 - \Delta T$ (see text) are approximated by the $Z = 1$ Coulomb phases, $\sigma_p^{<}$ and $\sigma_p^{>}$, respectively. The magnitude of the associated short-range phase shift in He is smaller than 0.05 rad. The inset shows the effect of neglecting the time-reversed contribution (B′) to the s and d wave in two-color ionization (dotted curve).

The calculations of two-photon ionization amplitude for He show that the dominant contribution to the variation of the atomic phase difference in the resonance region corresponds to diagram A. Nevertheless, a significant phase correction originates in the B and B′ pathways with the time-reversed process (B′) giving a non-negligible contribution to the s-wave electronic channel. On the other hand, the d-wave channel shows a smooth, nonresonant behavior of the phase with some deviations from the Coulombic approximation due to the onset of the nearby ${}^1D^e$ autoionizing resonances centered at higher electron kinetic energies. Obviously, the continuum–continuum phases corresponding to pathways B and B′ and the nonresonant pathways are much smaller than those related to pathway A and resonant ionization pathways. Therefore, not only is the photon interaction with a more energetic electron in the unstructured continuum less probable, but also the corresponding phase contribution to the two-photon ionization amplitude is lower.

3. EXPERIMENTAL RESULTS

To test our theoretical predictions, an experiment was performed at the low-density matter (LDM) beamline [40] using XUV pulses from the seeded FEL facility FERMI in Trieste, Italy. The 50 fs long, horizontally polarized light pulses propagated perpendicularly to the direction of the He gas pulses generated by an Even–Lavie valve in the horizontal plane (Fig. 4). Electrons emitted from the gas target were efficiently collected and observed by a magnetic bottle electron spectrometer (MBES) mounted vertically [41]. In the MBES, the electron trajectories are parallelized in the direction of the strong magnetic field gradient, and the kinetic energies of the electrons are determined by measuring their time of flight in the spectrometer's drift tube.

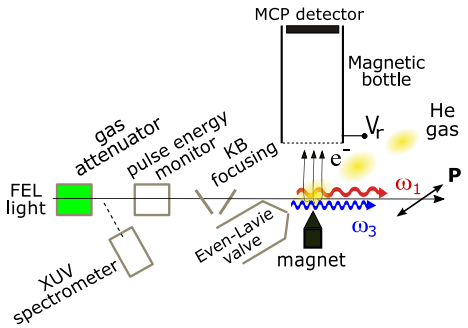

Fig. 4. Scheme of the experimental setup.

A. Single-Path Two-Photon Resonant Ionization

The wavelength of the FEL light was first scanned in the vicinity of 42.8 nm (28.9 eV) to locate the He $2s^2$ resonance via the two-photon $\omega_1 + \omega_1$ excitation path. The data points shown in Fig. 5 were recorded with 70 μJ FEL pulses generated by tuning all six FEL-1 undulators to ω_1. The resonant part of the electron signal originates from the autoionization decay of the $2s^2$ state,

$$\mathrm{He}(2s^2) \rightarrow \mathrm{e}^-(E_2) + \mathrm{He}^+(1s), \tag{6}$$

and is given by the yield of the spectral line centered at electron kinetic energy $E_2 = 2\omega_1 - T_1 \approx 33.2$ eV (Fig. 1), where $T_1 = 24.587$ eV is the ionization energy of the ground state He atom. In this measurement, a retardation potential (V_r) equal to −14 V was applied to the spectrometer's drift tube to block the detection of electrons with energy $E_1 = 4.3$ eV ejected by the dominant one-photon ionization process of the neutral He atom. A comparison with the calculated two-photon electron yield shows that the measured spectral profile of the resonance features an additional background and is slightly broader than the theoretical Fano profile. Convolution with a 30 meV broad Gaussian spectral function of the incoming light brings the calculated resonant two-photon ionization cross section into good agreement with the experimental shape, with the exception of the excess background.

The background signal in the resonance region is explained by the contribution of two spectroscopically unresolved nonresonant processes driven by the weak residual second- (ω_2) and third-order (ω_3) light generated simultaneously with the intense fundamental radiation at photon energy ω_1: one-photon ionization with ω_2 photons, and sequential double ionization of He with ω_1 and ω_3 photons. While ionization with ω_2 light generates a flat electron background at kinetic energies exactly coinciding with kinetic energies E_2 from the $2s^2$ autoionization (11), the electrons emitted in the second step of the sequential process have 0.9 eV lower kinetic energy $E_q = \omega_3 - T_2 \approx 32.3$ eV, where $T_2 = 54.418$ eV is the ionization energy of $\mathrm{He}^+(1s)$ (Fig. 1).

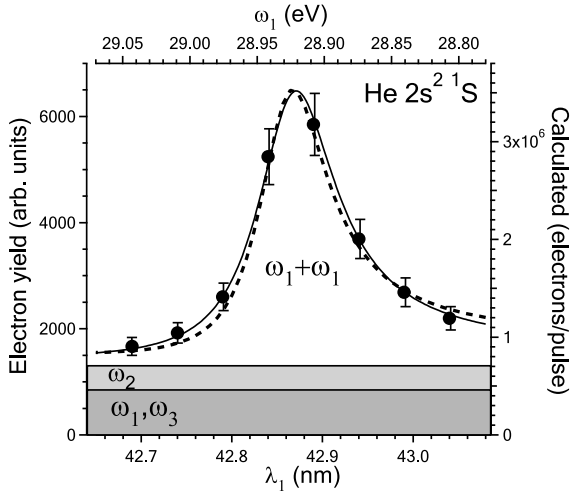

Fig. 5. The $\omega_1 + \omega_1$ electron yield in the energy region of the $2s^2$ resonance of He. The calculated electron yield [Eqs. (2) and (9), dashed black curve] describes well the experimental data (points), fitted by the Fano line shape (thin black curve). At the maximum experimental pulse intensity (10^{15} W/cm^2), the excess background level is reproduced by assuming an estimated 4.5% admixture of the second and third harmonic, and by considering the target volume effect.

B. Two-Path Two-Photon Resonant Ionization

In the second set of measurements, the population of the $2s^2$ state was observed while changing the phase of the ω_3 light with respect to the ω_1 light. To measure the interference effect, pulses with energies of a few μJ for each of the two colors were delivered to the target by tuning the first three FEL undulators to generate ω_1 light and the last three undulators to generate ω_3 light (Fig. 6).

To study the wavelength dependence of the two-color two-photon excitation, seven independent phase scans were made by tuning twice the light frequency ω_1 to five different positions along the $2s^2$ spectral profile. Phase φ of the electric field $\mathbf{F}_3$ of the third harmonic was varied by delaying the light-generating electron bunch in the magnetic chicane [21] before entering the second set of undulators. A complete φ-phase scan consists of 21 electron spectra that cover a 4π phase interval with equidistant sampling of φ. In the final experimental configuration, electrons in the spectrometer's drift tube were retarded by −29 V potential to resolve the sequential ionization signal P_q from the autoionization signal P_2 (Fig. 7). The only remaining peak in the electron spectrum was P_3 due to one-photon ionization with ω_3 light, resulting in

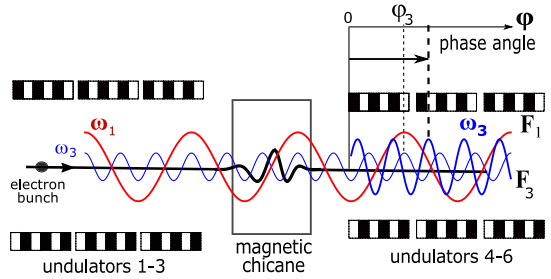

Fig. 6. The generation scheme of the coherent ω_1 (red curve) and ω_3 (blue curve) light pulses with a variable phase difference $\varphi - \varphi_3$. The first three FERMI FEL-1 undulator modules generated the ω_1 light with electric field $\mathbf{F}_1$ together with the weak third-harmonic light and the last three undulator modules generated ω_3 light with adjustable phase φ of the electric field $\mathbf{F}_3$ set by the delay of the electron bunch in the magnetic chicane.

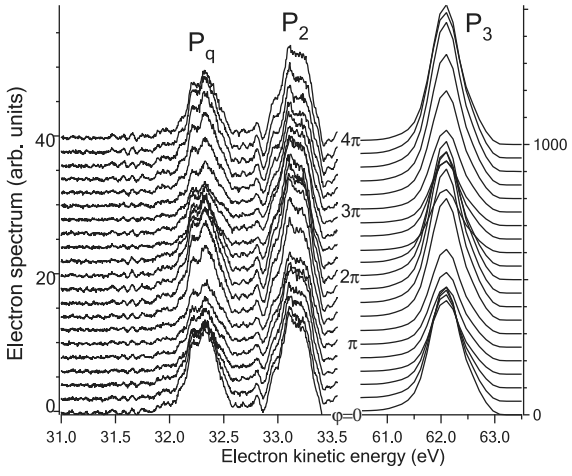

Fig. 7. Examples of electron spectra recorded at high retardation during a single phase scan with $2\omega_1 = 28.95$ eV corresponding to the top of the $2s^2$ resonance. The spectra acquired at different phase angles φ are vertically displaced. The FEL pulse energy at the target was approximately 10 μJ. The P_2 and P_q contributions to the electron yield correspond to electron kinetic energies E_2 and E_q, respectively. These two contributions are not resolved in the low-resolution electron spectra leading to the wavelength-dependent electron yield in the one-color experiment (Fig. 5).

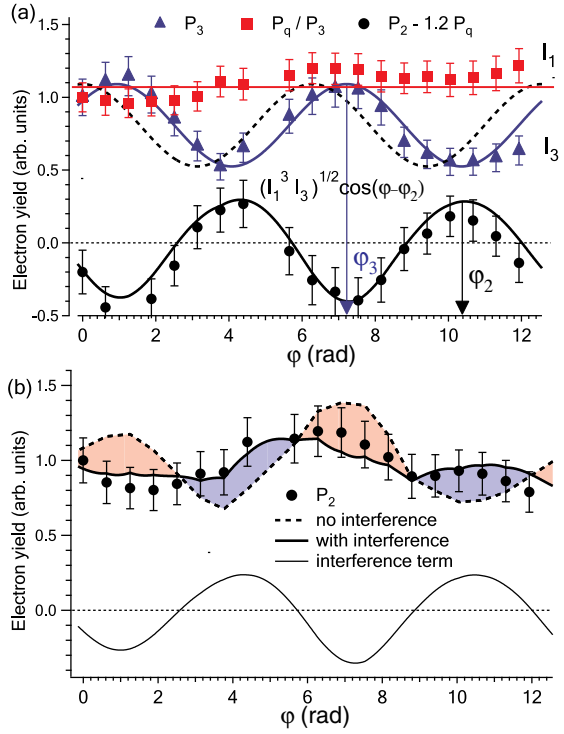

Fig. 8. (a) Top, the measured P_3 electron yield (triangles) and the experimental P_q/P_3 ratio, normalized to unity at $\varphi = 0$ (squares); bottom, weighted difference $P_2 - 1.2P_q$ (circles). The yields have been recorded at the center of the $2s^2$ two-photon resonance. The P_3 signal and the interference yield reach their respective maxima at phase angles φ_3 and φ_2. The dashed curve shows the cosine function with zero offset. (b) The measured P_2 yield (circles), decomposed into the direct and interference contributions obtained by fitting Eq. (13) to the experimental data.

photoelectrons with high kinetic energy $E_3 = \omega_3 - T_1 \approx 62.1$ eV (Fig. 1).

A strong sinusoidal modulation of the P_3 electron yield with phase angle φ was observed [Fig. 8(a)]. This is due to the weak residual ω_3 light produced in the first three undulators that was partially seeding the generation of ω_3 light in the second set of undulators. The intensity modulation of the emitted ω_3 light is proportional to $\cos(\varphi - \varphi_3)$, where φ_3 denotes the phase offset of the residual component. The intensity of the emitted third harmonic (I_3) reaches its maximum when the seeding is most efficient, i.e., when a delayed electron bunch generates light at a zero phase difference with respect to the residual ω_3 light. Our simulations show that the small admixture of the third harmonic in the first set of undulators is inphase with the fundamental radiation ω_1. The maximum of the $P_3(\varphi)$ signal then conveniently serves to determine the phase angle φ_3 (modulo 2π) at which the phase difference of emitted ω_1 and ω_3 light is zero.

The observed P_q electron yield closely follows the P_3 yield and *also* the intensity of the ω_1 light, as expected for the signal coming from a sequential double ionization with ω_1 and ω_3 photons. For long light pulses, for which the fields complete many cycles, the sensitivity of P_q to the electric field phase difference is lost, and the corresponding electron yield depends only on the product of the intensities ($I_1 I_3$) [42]. This is different for the P_2 signal because of the interference: according to Eq. (4), the $2s^2$ autoionization yield for given values of I_1 and I_3 is

$$y = M_<^2 I_1^2 + M_>^2 I_1 I_3 + 2M_< M_> \sqrt{I_1^3 I_3}\cos(\phi - \delta). \quad (7)$$

The positive quantities $M_<$ and $M_>$ and the atomic phase δ may be considered constant in a single phase scan using narrow-bandwidth pulses with the frequency centered at ω_1. As argued above, in an arbitrary phase reference frame against which φ is measured, the phase difference of the emitted ω_3 light with respect to the emitted ω_1 light is given by $\phi = \varphi - \varphi_3$, where φ_3 denotes the phase angle at which the P_3 electron yield reaches a maximum. At the same time, the theory predicts that atomic phase δ practically coincides with the phase difference of the two-photon ionization paths in the s-wave electronic channel in the resonance region.

The variation of light intensities during the phase scan, I_3 in particular, prevents a direct visualization of the characteristic shifted cosine dependence in the observed $P_2(\varphi)$ electron yield [Fig. 8(b)]. To isolate the signal modulation caused by the two-path interference, a data fit of the P_2 yield is required that relies on the simultaneously measured P_3 and P_q electron yields,

$$P_2 = \mathcal{A}(P_q/P_3)^2 + \mathcal{B}P_q + \mathcal{C}(P_q/P_3)\sqrt{P_q}\cos(\varphi - \varphi_2). \quad (8)$$

The above form has four fitting parameters: weights $\mathcal{A}, \mathcal{B}, \mathcal{C} > 0$, which correspond to the three terms in Eq. (7), and an offset phase angle, $\varphi_2 = \varphi_3 + \delta$. The latter allows one to uniquely determine the atomic phase δ when φ_3 is known. The offset angle φ_3 is obtained from the fit of the scaled and vertically offset $\cos(\varphi - \varphi_3)$ function to the measured $P_3(\varphi)$ yield.

In the absence of target volume effects, the P_3 signal is proportional to the integral of intensity of the third harmonic over the target volume and over the duration of the ω_3 pulse, i.e., to the total number of ω_3-photons impinging on the target. On the other hand, the experimental P_q/P_3 ratio is proportional to the number of ω_1-photons in the spatiotemporal region of the target that is occupied by ω_3 photons too. When the light pulses overlap only partially, the two-color light intensity ratio depends on time differently in different parts of the target. Under such conditions, weights $\mathcal{A}$ and $\mathcal{B}$ cannot be directly related to the probabilities of the corresponding two ionization paths in the single-atom case. For example, while the $\omega_1 + \omega_1$ ionization generates electrons in the target volume crossed by the ω_1 pulse, the electrons ejected by the $\omega_3 - \omega_1$ ionization are emitted only from the pulse overlap region. The interference weight ($\mathcal{C}$) also depends on the pulse overlap, but is more reliably determined due to the cosine factor in the fitting function, which makes uncertainties in the representation of the average light intensities less important. The phase offset parameter (φ_2) does not depend on the local variations of intensities and the atomic phase δ may be reliably extracted from the fit provided the phase difference of the two colors does not vary significantly in the pulse overlap target region. The fit of the phase scan data taken on top of the $2s^2$ resonance (Fig. 8) results in weights and phase offsets $\mathcal{A} + \mathcal{B} = 1.09 \pm 0.12, \mathcal{C} = 0.26 \pm 0.10$, $\varphi_3 = -0.94 \pm 0.25$ rad, and $\varphi_2 = 2.12 \pm 0.35$ rad, and leads to atomic phase $\delta = 3.22 \pm 0.60$ rad.

The observed P_q/P_3 trends indicate a relatively stable intensity of the ω_1 light during the phase scan, and a difference of up to a factor of 4 between the different scans. The variation of the average I_3 light intensity differed by no more than a factor of 2 between the scans, as shown by the P_3 signal trends. The extraction of the interference signal from the P_2 data enables an estimation of the interference contrast for each of the phase scans: the observed

contrasts lie between 0.1 and 0.5 and are found to increase with the average I_3/I_1 intensity ratio.

4. DISCUSSION

The atomic phases extracted from the fits are shown in Fig. 9 as a function of photon frequency ω_1. The measured points (blue filled, and red open circles) shows some agreement with the calculated curve (black curve), but there are some clear discrepancies in offset that must be resolved. First, two out of the three data points taken on the top of the resonance deviate from the measured trend by an additional $\Delta_a = 1.1 \pm 0.5$ rad. The corresponding two-phase scans were taken with the FEL light passing through a gas attenuator filled with the nitrogen gas at 6.3×10^{-3} mbar [43]. The 5 m long attenuator is located after the exit of the last undulator module and before the target (Fig. 4) and was empty when the other five phase scans were made. A straightforward calculation of phase velocities in nitrogen shows that ω_3 light acquires 1.3 rad phase delay with respect to the ω_1 light in the attenuator, very close indeed to the observed deviation Δ_a (see Supplement 1 for details). The observed phase shift corresponds to 9 as delay of the ω_3 wavefronts with respect to the ω_1 wavefronts and, if neglected, results in a value of the experimental atomic phase that is too high by Δ_a. It is well known that phase shifts due to light passing through a condensed matter play a major role in differential phase-contrast imaging with hard x rays [44,45] and XUV radiation [46].

The remaining phase offset $\Delta_g = 1.1 \pm 0.3$ rad of the whole experimental data set with respect to the calculated trend of atomic phase differences (see Fig. 9) is most likely due to a mismatch of the focal plane positions of the two light beams with different source positions, but focused by the same pair of KB mirrors (Fig. 4).

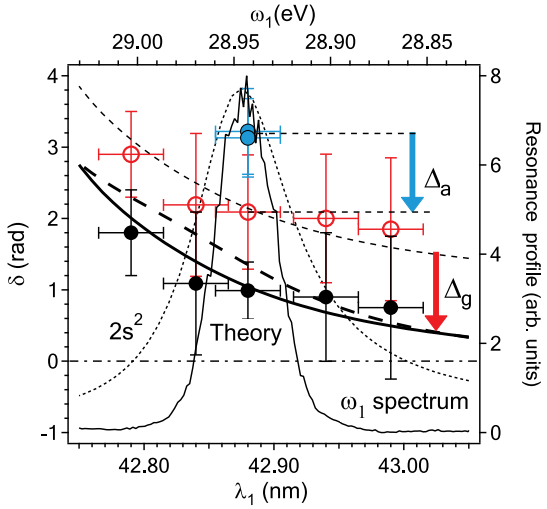

Fig. 9. The atomic phase difference δ as a function of photon energy ω_1 in the vicinity of He $2s^2\,{}^1S$ resonance. The two blue full circles refer to the phase scans with the nitrogen-filled gas attenuator and the empty red (gray) circles to the five phase scans made with an empty attenuator. By compensating the measured differences with the constant phase offsets due to the frequency-dependent light propagation velocity in the attenuator ($\Delta_a = 1.1$ rad) and different focal point position of ω_1 and ω_3 light ($\Delta_g = 1.1$ rad), the experimental atomic phase differences (black circles) agree very well with the calculated data (black curve). The agreement is worse if the calculation does not take into account the time-reversed $\omega_3 - \omega_1$ path (dashed curve). $2s^2$ resonance profile and the phase-scan-averaged spectrum of ω_1 light are depicted by black dotted and thin black curves, respectively (see Supplement 1 for details).

Our ray-tracing calculations show that the ω_1 light was focused 3 ± 1 mm before the target because the production of light by the first set of undulators placed the source point of ω_1 light upstream with respect to the source point of the ω_3 light generated by the second set of undulators, which was focused right on the target. Such a beam geometry leads to a Gouy phase delay of the ω_3 light with respect to the ω_1 light, and for this reason, the experimental trend of atomic phase differences appears too high by Δ_g. Simple considerations relying on the calculated beam profiles lead to an effective 0.4 rad geometrical phase difference of the two colors at the target (see Supplement 1 for details). We note that a considerable remaining difference from Δ_g does not invalidate a possible geometrical origin of the observed phase offset because the uncertainty of the estimate may still be larger due to notable deviations of our ray-tracing results (not providing the beam phase profiles) from the Gaussian beam propagation model, as well as due to not precisely known focal point positions with respect to the target.

Still, the above analysis provides confidence in the above interpretation, and permits a comparison of the measured interference contrast with the theoretical prediction. Experimentally, the contrast is found to increase with the ratio of the total number of ω_3 and ω_1 photons impinging on the target. However, this ratio was determined only on a relative scale, by monitoring the yield of ω_1 light pulses captured by the XUV spectrometer and by measuring the electron yield P_3 due to photoionization of He with ω_3 photons. In the absence of target saturation effects and for light pulses with equal shapes sharing the same focal plane, the photon number ratio is proportional to the ratio of peak intensities I_3/I_1 of the two light pulses at the target. A single scaling factor needed for absolute calibration of the experimental photon number ratio was obtained by matching the experimental trend to the calculated I_3/I_1 dependence of the interference contrast for the Gaussian-shaped beams. Relying on the measured ω_1 pulse energies and on the estimated defocusing of the ω_1 beam at the target (2.5 times the beam waist diameter), the calibration procedure results in reasonable values of I_3 up to about 10^{13} W/cm^2 when $I_3/I_1 \approx 0.8$. Since I_1 was not higher than 3×10^{13} W/cm^2, the target saturation effects in our two-color measurements were indeed negligible (see Supplement 1 for details).

5. CONCLUSIONS

Using the intense, tunable, and coherent XUV light pulses provided by the FERMI FEL, and owing to the efficient electron collection, filtering, and spectral resolution of the magnetic bottle spectrometer, we have measured the spectral profile of the $2s^2\,{}^1S^e$ autoionizing resonance in He. The state was populated by one-color two-photon absorption $\omega_1 + \omega_1$, and the acquired spectrum agrees very well with the calculated two-photon ionization yield in the energy region of the resonance. By adding the $\omega_3 - \omega_1$ two-photon path to the excitation scheme and by varying the relative phase of ω_1 and ω_3 photon fields, the population of the resonance state was modulated by the two-path interference. The phase difference at which the two paths interfere constructively is characterized by a maximum population of the resonance state and equals the phase difference of the two-photon atomic amplitudes. The observed trend of atomic phase differences in the resonance spectral region agrees very well with the calculated trend when a small phase velocity mismatch of the two colors in the gas attenuator is considered and the theory accounts for the time-reversed $-\omega_1 + \omega_3$ excitation path. Good agreement with the theory on

an absolute scale is obtained only when the experimental data are corrected with a constant phase offset stemming from different focusing of the ω_1 and ω_3 beams in the target region. The presented approach is a development of previous all-optical coherent-control experiments and RABBITT experiments, entering the XUV wavelength range, and demonstrates the possibility of calculating and measuring the phase difference of multiphoton excitation paths connecting energetically distant intermediate states by observing final state populations only.

Finally, the two-path experimental configuration forms an atomic XUV interferometer, where an ensemble of atoms delivers a maximum response in terms of the emitted electron yield when the phase difference of the ω_1 and ω_3 light equals an atom-specific value for the selected pair of light frequencies. When an optical element is inserted into the light path and causes an extra phase difference of the two colors, the generated phase shift can be measured by observing a displacement of the maximum of the interference signal in the same phase reference frame. Since the interference of the $\omega_1 + \omega_1$ and $\omega_3 - \omega_1$ paths persists in the unstructured electronic continuum, such an atomic interferometer enables measurements also at frequencies far away from the resonant condition (although with a considerable experimental effort) because of the lower electron yields. The atomic phase difference does not depend on light intensities, but the electron yield does, and it is important to monitor single-color light intensities during the phase scan to reliably identify the phase angle with the maximum interference contribution to the yield. Similar to other interferometric setups, the quality and precision of these experiments essentially depends on the definition and stability of the spatiotemporal overlap of the ω_1 and ω_3 light pulses in the target.

Funding. Javna Agencija za Raziskovalno Dejavnost RS (P1-0112); Horizon 2020 Framework Programme (730872); Institut "Jožef Stefan".

Acknowledgment. This work was financially supported by the Slovenian Research Agency in the framework of research programme "Studies of Atoms, Molecules and Structures by Photons and Particles." The research leading to these results has received funding from the Horizon 2020 European Community's Programme. We thank the PADReS team for the superb beam alignment and focusing.

Disclosures. The authors declare no conflicts of interest.

Data availability. Data underlying the results presented in this paper are not publicly available at this time but may be obtained from the authors upon reasonable request.

Supplemental document. See Supplement 1 for supporting content.

REFERENCES

1. P. B. Corkum, "Plasma perspective on strong field multiphoton ionization," Phys. Rev. Lett. **71**, 1994–1997 (1993).
2. J. Itatani, F. Quéré, G. L. Yudin, M. Y. Ivanov, F. Krausz, and P. B. Corkum, "Attosecond streak camera," Phys. Rev. Lett. **88**, 173903 (2002).
3. H. G. Muller, "Reconstruction of attosecond harmonic beating by interference of two-photon transitions," Appl. Phys. B **74**, s17–s21 (2002).
4. M. Isinger, D. Busto, S. Mikaelsson, S. Zhong, C. Guo, P. Salieres, C. L. Arnold, A. L'Huillier, and M. Gisselbrecht, "Accuracy and precision of the RABBIT technique," Philos. Trans. R. Soc. A. **377**, 20170475 (2019).
5. K. Klünder, J. M. Dahlström, M. Gisselbrecht, T. Fordell, M. Swoboda, D. Guénot, P. Johnsson, J. Caillat, J. Mauritsson, A. Maquet, R. Taeb, and A. L'Huillier, "Probing single-photon ionization on the attosecond time scale," Phys. Rev. Lett. **106**, 143002 (2011).
6. A. Chacon, M. Lein, and C. Ruiz, "Asymmetry of Wigner's time delay in a small molecule," Phys. Rev. A **89**, 053427 (2014).
7. L. Gallmann, I. Jordan, H. J. Wörner, L. Castiglioni, M. Hengsberger, J. Osterwalder, C. A. Arrell, M. Chergui, E. Liberatore, U. Rothlisberger, and U. Keller, "Photoemission and photoionization time delays and rates," Struct. Dyn. **4**, 061502 (2017).
8. J. Dahlström, D. Guénot, K. Klünder, M. Gisselbrecht, J. Mauritsson, A. L'Huillier, A. Maquet, and R. Taïeb, "Theory of attosecond delays in laser-assisted photoionization," Chem. Phys. **414**, 53–64 (2013).
9. C. K. Chan, P. Brumer, and M. Shapiro, "Coherent radiative control of IBr photodissociation via simultaneous (ω_1,ω_3) excitation," J. Chem. Phys. **94**, 2688–2696 (1991).
10. X. Wang, R. Bersohn, K. Takahashi, M. Kawasaki, and H. L. Kim, "Phase control of absorption in large polyatomic molecules," J. Chem. Phys. **105**, 2992–2997 (1996).
11. M. Shapiro and P. Brumer, *Control of Molecular Processes*, 2nd ed. (Wiley, 2012).
12. E. A. Seddon, J. A. Clarke, D. J. Dunning, C. Masciovecchio, J. Milne, F. Parmigiani, D. Rugg, J. C. H. Spence, N. R. Thompson, K. Ueda, S. M. Vinko, J. S. Wark, and W. Wurth, "Short-wavelength free-electron laser sources and science: a review," Rep. Prog. Phys. **80**, 115901 (2017).
13. E. Allaria, R. Appio, L. Badano, *et al.*, "Highly coherent and stable pulses from the FERMI seeded free-electron laser in the extreme ultraviolet," Nat. Photonics **6**, 699–704 (2012).
14. K. C. Prince, E. Allaria, C. Callegari, *et al.*, "Coherent control with a short-wavelength free-electron laser," Nat. Photonics **10**, 176–179 (2016).
15. D. You, K. Ueda, E. V. Gryzlova, *et al.*, "New method for measuring angle-resolved phases in photoemission," Phys. Rev. X **10**, 031070 (2020).
16. C. Chen, Y.-Y. Yin, and D. S. Elliott, "Interference between optical transitions," Phys. Rev. Lett. **64**, 507–510 (1990).
17. Y.-Y. Yin, C. Chen, D. S. Elliott, and A. V. Smith, "Asymmetric photoelectron angular distributions from interfering photoionization processes," Phys. Rev. Lett. **69**, 2353–2356 (1992).
18. N. B. Baranova, B. Y. Zel'dovich, A. N. Chudinov, and A. A. Shul'ginov, "Theory and observation of polar asymmetry of photoionization in a field with $\langle E^3\rangle \neq 0$," Sov. Phys. JETP **71**, 1043 (1990).
19. N. B. Baranova and B. Y. Zel'dovich, "Physical effects in optical fields with nonzero average cube, $\langle E^3\rangle \neq 0$," J. Opt. Soc. Am. B **8**, 27–32 (1991).
20. N. B. Baranova, I. Beterov, B. Y. Zel'dovich, I. Ryabtsev, A. N. Chudinov, and A. A. Shul'ginov, "Observation of an interference of one- and two-photon ionization of the sodium 4s state," JETP Lett. **55**, 439 (1992).
21. B. Diviacco, R. Bracco, D. Millo, and M. M. Musardo, "Phase shifters for the FERMI at Elettra undulators," in *2nd International Particle Accelerator Conference (IPAC)* (JACoW, 2011), pp. 3278–3280.
22. M. Swoboda, T. Fordell, K. Klünder, J. M. Dahlström, M. Miranda, C. Buth, K. J. Schafer, J. Mauritsson, A. L'Huillier, and M. Gisselbrecht, "Phase measurement of resonant two-photon ionization in helium," Phys. Rev. Lett. **104**, 103003 (2010).
23. M. Sabbar, S. Heuser, R. Boge, M. Lucchini, T. Carette, E. Lindroth, L. Gallmann, C. Cirelli, and U. Keller, "Resonance effects in photoemission time delays," Phys. Rev. Lett. **115**, 133001 (2015).
24. V. Gruson, L. Barreau, A. Jiménez-Galan, F. Risoud, J. Caillat, A. Maquet, B. Carré, F. Lepetit, J.-F. Hergott, T. Ruchon, L. Argenti, R. Taeb, F. Martín, and P. Salières, "Attosecond dynamics through a Fano resonance: monitoring the birth of a photoelectron," Science **354**, 734–738 (2016).
25. D. Busto, L. Barreau, M. Isinger, M. Turconi, C. Alexandridi, A. Harth, S. Zhong, R. J. Squibb, D. Kroon, S. Plogmaker, M. Miranda, Á. Jiménez-Galán, L. Argenti, C. L. Arnold, R. Feifel, F. Martín, M. Gisselbrecht, A. L'Huillier, and P. Salières, "Time–frequency representation of autoionization dynamics in helium," J. Phys. B **51**, 044002 (2018).
26. C. Cirelli, C. Marante, S. Heuser, *et al.*, "Anisotropic photoemission time delays close to a Fano resonance," Nat. Commun. **9**, 955 (2018).
27. L. Barreau, C. L. M. Petersson, M. Klinker, A. Camper, C. Marante, T. Gorman, D. Kiesewetter, L. Argenti, P. Agostini, J. González-Vázquez, P. Salières, L. F. DiMauro, and F. Martín, "Disentangling spectral phases of interfering autoionizing states from attosecond interferometric measurements," Phys. Rev. Lett. **122**, 253203 (2019).
28. A. Jiménez-Galán, L. Argenti, and F. Martín, "Modulation of attosecond beating in resonant two-photon ionization," Phys. Rev. Lett. **113**, 263001 (2014).
29. A. Jiménez-Galán, F. Martín, and L. Argenti, "Two-photon finite-pulse model for resonant transitions in attosecond experiments," Phys. Rev. A **93**, 023429 (2016).

30. L. Argenti, A. Jiménez-Galán, J. Caillat, R. Taïeb, A. Maquet, and F. Martín, "Control of photoemission delay in resonant two-photon transitions," Phys. Rev. A **95**, 043426 (2017).
31. M. Vacher, R. Gaillac, A. Maquet, R. Taïeb, and J. Caillat, "Transition dynamics in two-photon ionisation," J. Opt. **19**, 114011 (2017).
32. U. Fano, "Effects of configuration interaction on intensities and phase shifts," Phys. Rev. **124**, 1866–1878 (1961).
33. J. Z. E. Cormier and H. Bachau, "Discretization techniques applied to the study of multiphoton excitation of resonances in helium," J. Phys. B **26**, 4449–4463 (1993).
34. E. C. I. Sánchez and H. Bachau, "Theory of two-photon spectroscopy of autoionizing states in helium and beryllium," J. Phys. B **28**, 2367–2384 (1995).
35. J.-M. R. A. Burgers and D. Wintgen, "Highly doubly excited S states of the helium atom," J. Phys. B **28**, 3163–3183 (1995).
36. A. Mihelič, "Role of intermediate continuum states in exterior complex scaling calculations of two-photon ionization cross sections," Phys. Rev. A **98**, 023409 (2018).
37. A. Mihelič and M. Horvat, "Calculation of multiphoton ionization amplitudes and cross sections of few-electron atoms," Phys. Rev. A **103**, 043108 (2021).
38. U. D. Jentschura, "Nonresonant two-photon transitions in length and velocity gauges," Phys. Rev. A **94**, 022117 (2016).
39. Á. J. Galán, L. Argenti, and F. Martín, "The soft-photon approximation in infrared-laser-assisted atomic ionization by extreme-ultraviolet attosecond-pulse trains," New J. Phys. **15**, 113009 (2013).
40. C. Svetina, C. Grazioli, N. Mahne, *et al.*, "The low density matter (LDM) beamline at FERMI: optical layout and first commissioning," J. Synchrotron Radiat. **22**, 538–543 (2015).
41. F. Penent, J. Palaudoux, P. Lablanquie, L. Andric, R. Feifel, and J. H. D. Eland, "Multielectron spectroscopy: the Xenon 4D hole double Auger decay," Phys. Rev. Lett. **95**, 083002 (2005).
42. W.-C. Jiang, W.-H. Xiong, T.-S. Zhu, L.-Y. Peng, and Q. Gong, "Double ionization of He by time-delayed attosecond pulses," J. Phys. B **47**, 091001 (2014).
43. L. Rumiz, D. Cocco, C. Fava, S. Gerusina, R. Gobessi, E. Mazzucco, and F. Zudini, "The gas attenuator vacuum system of Fermi/Eletttra," in *2nd International Particle Accelerator Conference (IPAC)* (JACoW, 2011), p. 1530.
44. T. J. Davis and A. W. Stevenson, "Direct measure of the phase shift of an x-ray beam," J. Opt. Soc. Am. A **13**, 1193–1198 (1996).
45. S. Mayo and M. Endrizzi, "X-ray phase contrast methods," in *Handbook of Advanced Nondestructive Evaluation*, N. Ida and N. Meyendorf, eds. (Springer, 2019), pp. 1053–1093.
46. M. Zürch and C. Spielmann, "Extreme ultraviolet digital in-line holography using a tabletop source," Appl. Opt. **54**, 5992–5997 (2015).